Electrochimica Acta 75 (2012) 239–246

Contents lists available at SciVerse ScienceDirect

Electrochimica Acta

journal homepage: www.elsevier.com/locate/electacta

Modeling discharge deposit formation and its effect on lithium-air battery performance

Yun Wang*

Renewable Energy Resources Lab (RERL), Department of Mechanical and Aerospace Engineering, The University of California, Irvine, CA 92697-3975, United States

ARTICLE INFO

Article history:
Received 29 March 2012
Received in revised form 28 April 2012
Accepted 28 April 2012
Available online 12 May 2012

Keywords:
Lithium-air battery
Discharge deposit
Passiviation
Modeling
PEM fuel cells
Ice formation

ABSTRACT

Lithium-air batteries show a great promise in electrochemical energy storage with their theoretical specific energy comparable to gasoline. Discharge products such as Li_2O_2 or Li_2CO_3 are insoluble in several major nonaqueous electrolytes, and consequently precipitate at the reaction sites. These materials are also low in electric conductivity. As a result, the reduced pore space and electrode passiviation increase the reaction resistance and consequently reduce discharge voltage and capability. This work presents a modeling study of discharge product precipitation and effects for lithium-air batteries. Theoretical analysis is also performed to evaluate the variations of important quantities including temperature, species concentrations, and electric potentials. Precipitation growth modes on planar, cylindrical and spherical surfaces are discussed. A new approach, following the study of ice formation in PEM fuel cells, is proposed. Validation is carried out against experimental data in terms of discharge voltage loss.

1. Introduction

Due to the growing concerns on fossil fuels' depletion and climate change, lithium-based battery technologies have received a great deal of attention in recent years owing to their relatively high efficiency and energy density. A successful example is lithium-ion batteries that have been widely used in nowadays portable and automotive applications. A major hurdle to battery development, however, is the insufficient low energy capability as opposed to fossil fuels. The gasoline's specific energy is about 13,000 Wh/kg, an order-of-magnitude higher than that of Li-ion batteries. Li-air batteries are an emerging area, showing a great promise of high specific energy storage. Their unique feature is that the cathode active material – oxygen is not stored inside the batteries, but obtained from the ambient environment. In addition, pure lithium metal, rather than Li intercalated graphite (LiC_6) as that in Li-ion batteries, is used as the anode material. The open circuit potential (OCP) of Li-air batteries can reach around 3.0 V. As a result, the theoretical specific energy reaches around 11,680 Wh/kg, comparable to gasoline and higher than methanol [1]. Fig. 1 shows schematic of a Li-air battery and its operation. Prior to their full commercialization stage, however, many scientific and technical challenges must be overcome.

Early concept of Li-air batteries can be traced back to the 1970s, originally proposed for automotive applications [2]. Abraham and Jiang reported one of the first nonaqueous Li-air batteries that show rechargeability [3]. The electrode and electrolyte are laminated to produce a battery of about 300 μm thick. The cell can be recharged when using cobalt phthalocyanine catalyst. In recent years, Li-air batteries received a growing interest of research and development. Most studies were focused on material design and performance characterization for the cathodes [4–10]. A major challenge in the cathode is the precipitation of discharge product such as Li_2O_2 and Li_2CO_3. These materials have low solubility in several major electrolytes, therefore are deposited over the reaction surface during discharging operation. These discharge products are poor electric conductors, leading to passivation, and increase reaction resistance. As the product accumulates in the cathode electrode with time, the discharge voltage drops (see Fig. 2). Several studies have attempted to understand the discharge product's effects. Albertus et al. presented both experimental and modeling studies on Li-air batteries with a special effort on investigating discharge product effect [11]. They used both flat and porous electrodes in experiment. They showed the cell voltage starts around 2.6 V, followed by a gradual decrease at initial stage and a rapid drop when close to 2.0 V. Their modeling followed the approach of lithium-ion batteries and accounted for the passiviation effect. Viswanathan et al. studied the electric conductivity of Li_2O_2 both experimentally and theoretically [12]. They treated the charge transport in the Li_2O_2 film following that in a biased metal insulator metal (MIM) junction. A Fc/Fc+ redox couple [13] was used to probe the electric

* Tel.: +1 949 824 6004; fax: +1 949 824 8585.
E-mail address: yunw@uci.edu

0013-4686/$ – see front matter © 2012 Elsevier Ltd. All rights reserved.
http://dx.doi.org/10.1016/j.electacta.2012.04.137

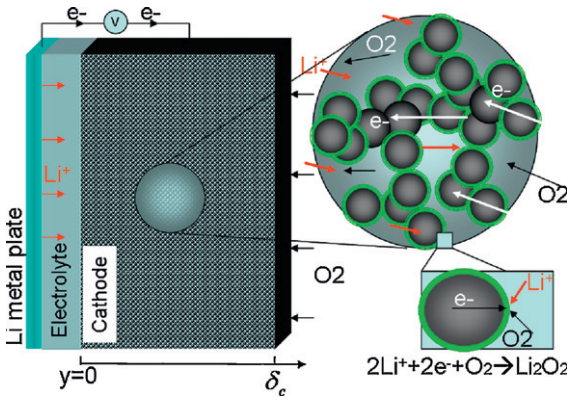

Fig. 1. Schematic of a Li-air battery and its discharge operation with discharge product Li_2O_2 as an example.

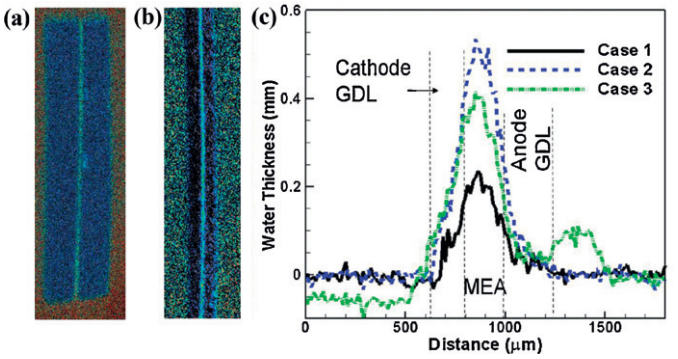

Fig. 3. Neutron images of ice formation in a fuel cell: (a) water content neutron image; (b) close-up image; and (c) water thickness in the PEFC detected by high-resolution neutron imagery. Cases 1–3: Cooling from 100, 50, 50% RH and cold start at 0.04, 0.04, and 0.094 A/cm^2, respectively [17].

resistance. They indicated that electron tunneling [14,15] may play an important role in sustaining the cathode electrochemical activity.

In polymer electrolyte fuel cells (PEFCs, also called PEM fuel cells), a similar phenomenon occurs under subfreezing condition, i.e. ice formation. Water is a byproduct of PEFCs by the oxygen reaction reduction (ORR) [16]. At subfreezing temperature, product water freezes to form ice, which is deposited in the electrode and causes cell voltage loss (see Figs. 3 and 4; [17]). Fig. 3 shows the evidence of ice accumulation in fuel cell electrodes. As a result of ice formation, the voltage decreases (as shown in Fig. 4). A theory has been developed to delineate various mechanisms of voltage loss caused by ice formation [18,19]. In this paper, we will also examine the effects of discharge product formation in Li-air batteries by extending the knowledge of PEFCs to Li-air batteries. Analysis will be performed on the spatial variations of important quantities such as species concentrations, temperature, and phase potentials. Comparison with literature experimental data will be presented. The results benefit both Li-air battery and PEFC developments.

2. Theoretical analysis

Lithium metal is used as the anode active material. Li dendrite/moss formation may occur upon battery cycling due to the preferential deposition of lithium metal, which may lead to shorts between the anode and cathode. A thin Li^+-conductive artificial layer is usually used to improve lithium anode stability. During discharge, the following electrochemical reaction occurs at the lithium–electrolyte interface:

$$\mathrm{Li(metal)} \rightarrow \mathrm{Li^+ + e^-} \tag{1}$$

The produced Li ions transport through the thin artificial layer and electrolyte to the cathode. The produced electrons are conducted through out circuit toward the cathode, where they combine with Li^+ ions and oxygen to form Li oxides or Li-based composites depending on the cathode electrochemistry detail. The battery electrolyte plays a critical role in determining the cathode electrochemistry. Li_2O_2 and Li_2CO_3 are the primary products when using several major nonaqueous electrolytes, e.g. organic and carbonate solvents, respectively. The exact reaction routes can be complex, involving several intermediates. The overall cathode reactions with Li_2O_2 and Li_2CO_3, respectively, as product can be rewritten by [1,3,11,12]:

$$\begin{aligned} &2\mathrm{Li^+} + \mathrm{O_2} + 2\mathrm{e^-} \rightarrow \mathrm{Li_2O_2(solid)} \\ &\mathrm{PC} + \mathrm{O_2} + n\mathrm{Li^+} + n\mathrm{e^-} \rightarrow \mathrm{Li_2CO_3(solid)} + \text{Li alkyl carbonates} + \text{other products} \end{aligned} \tag{2}$$

Both Li_2O_2 and Li_2CO_3 are usually insoluble in the corresponding electrolytes and exhibit low electric conductivity. As a result, the discharge materials are deposited over the carbon surface and form a thin film, hampering species transport and the electrochemical activity, and leads to cell voltage loss.

During discharging, irreversible processes occur, reducing the energy conversion efficiency. Comparing with Li-ion batteries, the operating efficiency of current Li-air battery technology is relatively low, around 50%. The rest of the energy is released in form of waste heat. Temperature has profound effects on Li-air battery performance due to its importance on overcoming the activation barriers of reactions. The principle mechanisms include the reversible, irreversible, and ohmic heating. The reversible and irreversible sources are released at the reaction interface during energy conversion, whereas the ohmic heating arises from the resistance to the electric current flows including ion movement. These sources lead to spatially varying temperature inside a battery. To evaluate the upper bound of temperature variation, one can assume all the heating sources were uniformly distributed inside the electrode, the temperature variation can be evaluated by [18]:

$$\Delta T = \frac{I(E_0 - V_{\mathrm{cell}})\delta_c}{2k^{\mathrm{eff}}} \tag{3}$$

where E_0 is defined as $-\Delta\bar{h}/2F$ and represents the EMF (electromotive force) that all the energy from Li–oxygen reaction, the 'calorific value', heating value, or enthalpy of formation, were transformed into electrical energy. The effective thermal conductivity of

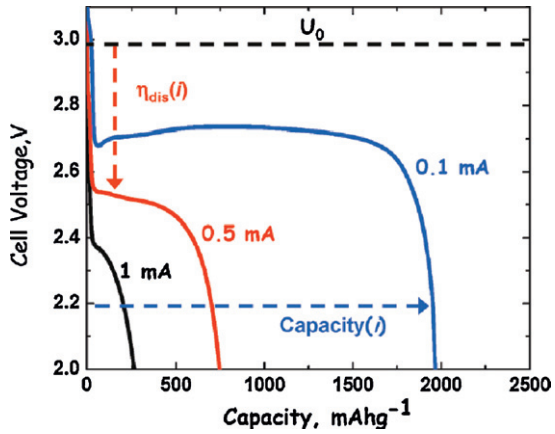

Fig. 2. Discharge curves at different current densities [1].

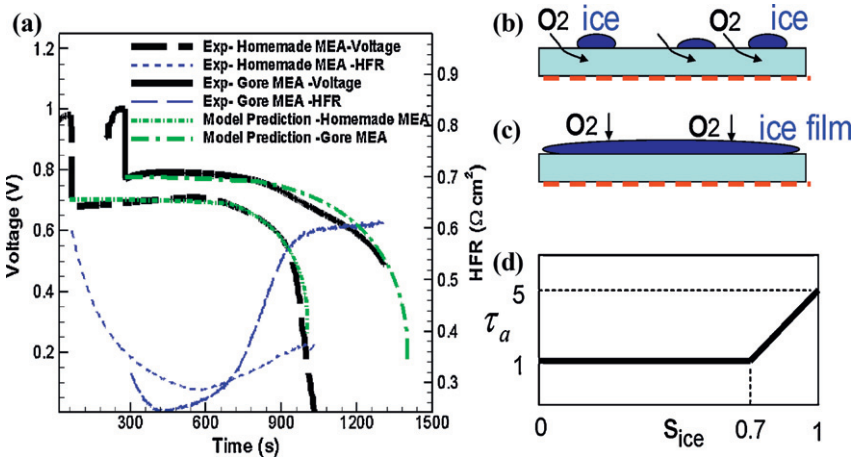

Fig. 4. (a) Cell voltages and HFR (high frequency resistance) of subfreezing operations at 0.02 A/cm^2 and -10 °C for PEFCs; (b) solid water islands scatter over the thin ionomer film, allowing oxygen access to the catalyst (dashed line); (c) ice islands connect, forming thin ice layer and blocking oxygen access to local catalyst; and (d) the factor of the ice coverage τ_a used in the model validation [17].

the cathode k^{eff} is determined by the material composition and structure, and can be evaluated by:

$$k^{\text{eff}} = \sum_{i=1}^{n} \varepsilon_i^{\tau_i} k_i \tag{4}$$

where ε_i and τ_i are the volume fraction and tortuosity of constituent material i in the cathode electrode, respectively. Among the materials, carbon and metal support such as Ni mesh are good thermal conductors, and the electrode effective thermal conductivity can be approximated by considering those materials only. To obtain a general sense of the temperature variation scale, k^{eff} of 1.0 W/(m K), 2.5 V, and 1 mA/cm^2 will yield around 0.01 °C variation. However, a higher current of 0.1 A/cm^2 will lead to an about 1 °C variation.

During discharging, the reactants of Li^+, oxygen, and electron are consumed. The primary driving forces for their transport are the gradients of their concentrations (for Li^+ and oxygen) and electric phase potentials (for ions and electrons). Assuming diffusion is the dominant force for the former two species, their spatial variations, in absence of bulk flow in the electrolyte, can be evaluated through:

$$\frac{\Delta C_e}{C_{e,0}} = \frac{(1-t_+^0)I}{2F}\frac{\delta_c}{C_{e,0}D_{Ce}^{\text{eff}}} \quad \text{or} \quad \Delta C_e = \frac{(1-t_+^0)I}{2F}\frac{\delta_c}{D_{Ce}^{\text{eff}}} \tag{5}$$

and

$$\frac{\Delta C_{O_2}}{C_{O_2,1}} = \frac{I}{8F}\frac{\delta_c}{C_{O_2,1}D_{O_2}^{\text{eff}}} \quad \text{or} \quad \Delta C_{O_2} = \frac{I}{8F}\frac{\delta_c}{D_{O_2}^{\text{eff}}} \tag{6}$$

where $C_{e,0}$ and $C_{O_2,1}$ are the concentrations of Li^+ and oxygen at $y = 0$ and $y = \delta_c$ (see Fig. 1), respectively. t_+^0 is the transference number of the Li^+ with respect to the velocity of solvent. Depending on the electrolyte composition, it can be a function of the electrolyte concentration. The effective coefficients of material properties can be evaluated through the Bruggeman correlation:

$$D_{Ce}^{\text{eff}} = \varepsilon^{\tau} D_{Ce}^0 \quad \text{and} \quad D_{O_2}^{\text{eff}} = \varepsilon^{\tau} D_{O_2}^0 \tag{7}$$

The O_2 diffusivity and solubility depends on the electrolyte material and composition. Read et al. [8] measured the solubility in several typical electrolytes. Its magnitude is around 0.00876 M in DME with 0.1 M Li^+ and 0.0021 M in PC of 1 M Li^+. The diffusivity in DME is around 4×10^{-5} cm^2/s and is about order of magnitude lower in PC (2.2×10^{-6} cm^2/s) [10]. Using the scale of the above diffusivity, the oxygen concentration variation will be around 0.01 and 0.1 mol/m^3 for the above DME and PC, respectively, τ of 1.5, δ_c of 0.001 mm and 1 mA/cm^2.

The oxygen diffusivity in the mixture for liquid electrolytes can be evaluated using a hydrodynamic model, which assumes that the resistance of solute molecule movement is caused by the viscous force, similar to a particle movement in a viscous fluid. In a dilute liquid, the approach will yield the famous Stokes–Einstein equation:

$$D^0 = \frac{k_B T}{6\pi r \mu} \tag{8}$$

where k_B is the Boltzmann's constant, r the radius of the oxygen molecule, and μ the electrolyte viscosity. In a solution that is not infinitely dilute, a modification could be made by introducing volume fraction of solute ε_i [20,21]:

$$D^{0*} = D^0(1 + 1.45\varepsilon_i) \tag{9}$$

The electric phase potentials will develop in both the electrolyte and carbon. Assuming C_e is almost uniform and its gradient is negligible, the electrolyte phase potential variation is caused by the ohmic resistance, estimated by:

$$\Delta\Phi^{(m)} = \frac{I\delta_c}{2\kappa^{\text{eff}}} \tag{10}$$

where the effective ionic conductivity κ^{eff} is relevant to the local volume fraction of the electrolyte in the electrode:

$$\kappa^{\text{eff}} = \varepsilon^{\tau_e}\kappa \tag{11}$$

The above adopts the Bruggeman correlation and usually τ_e can be empirically set to 1.5 when the exact pore structure is unknown. κ can be determined experimentally.

The electronic phase potential variation can be evaluated in a similar way using the ohmic law:

$$\Delta\Phi^{(s)} = \frac{I\delta_c}{2\sigma^{\text{eff}}} \tag{12}$$

where σ^{eff} can be empirically evaluated by accounting for the volume fraction of electric conductivity material or directly through experiment. In Ref. [11], a value of 10 S/m is suggested, which yields a variation of 0.001 V at 1 mA/cm^2 and δ_c of 1 mm. This magnitude is negligible as opposed to the battery's operating voltage. However, at higher current, e.g. 0.1 A/cm^2, or poorer conductor, the variation can be considerable and the resistance arises as a major factor limiting battery performance.

In all the above variations, two factors, besides the material properties, play an important role, they are the operating

current density I and cathode electrode thickness δ_c. Under common operating conditions such as 1 mA/cm^2 and δ_c of 1 mm and the materials currently used in many Li-air batteries, several variations are considerable, leading to a spatially varying reaction rate. Under the extreme condition of sufficiently small I and δ_c, the spatial variations can be diminished and the quantities can be treated as uniform. As a result, the reaction is homogeneous everywhere across the electrode. Further, flat electrodes have been used in experiment batteries to characterize the electrochemistry at the reaction surface [11,12]. As the reaction surface becomes perfectly planar, δ_c becomes zero and there exists no variations across the reaction site.

As explained before, the actual electrochemical reaction kinetics and path can be complex because a number of reaction steps and intermediates involve. In the cathode, the oxygen reduction reaction (ORR) occurs. For the ORR at the glassy carbon surface, the following steps may take place [22,23]: $O_2 \rightarrow O_{2(ads)}$; $O_{2(ads)} + e^- \rightarrow [O_{2(ads)}]^-$; $[O_{2(ads)}]^- \rightarrow O_{2(ads)}{}^-$; $O_{2(ads)}{}^- + H_2O \rightarrow HO_{2(ads)} + OH^-$; $HO_{2(ads)} + e^- \rightarrow HO_{2(ads)}{}^-$; $HO_{2(ads)}{}^- \rightarrow HO_2{}^-$. The subscripts "ads" denotes adsorption at the reaction surface. The third step was found to be the rate determining step for pH > 10; otherwise, the second was, as suggested by Taylor and Humffray [24,25]. For the sake of simplification, we assume a one-step reaction and approximated the discharge reaction rate by the Tafel equation:

$$j_c = -ai_c = -ai_{0,c}^{\mathrm{ref}} C_{O_2}^{1-\beta} C_e^{1-\beta} \exp\left(-\frac{1-\beta}{RT} F\eta\right) \tag{13}$$

where the factor of the surface-to-volume ratio a characterizes the roughness of porous electrodes. The Tafel equation is an approximation of the Butler–Volmer equation when a large surface overpotential is present which holds true for the cathode ORR of the battery. This is also similar to that of the PEM fuel cell cathode, where the ORR is sluggish and results in a large overpotential. The surface overpotential η is determined by the local phase potentials and equilibrium potential U_0:

$$\eta = \Phi^{(s)} - \Phi^{(m)} - U_0 \tag{14}$$

The above assumes no insoluble discharge products are deposited at the reaction surface. Again, for the extreme condition of negligible spatial variations of temperature, phase potentials, oxygen concentration, and C_e, the exchange current density j_c can be assumed to be uniformly distributed across the cathode.

3. Mathematical modeling

Insoluble discharge product will be deposited at local reaction sites. It is likely the initial precipitation nucleates heterogeneously at preferred sites, followed by thin film formation over the surface. Film formation was experimentally observed in flat electrodes. The deposit film has low electric conductivity, resisting electrons to react with Li^+ and oxygen. Fig. 5 shows several typical morphologies of film growth. The deposit film will grow as discharging proceeds. The film thickness is determined by the specific morphology of the deposited surface.

3.1. Film resistor model

3.1.1. Cylindrical-film growth mode

Sandhu et al. examined the limiting factor of oxygen transport in Li-air batteries [26]. They assumed the cathode pore network follows the cylindrical shape with a tortuosity. The reaction surface is the channel internal wall, where the reaction product is deposited, forming a cylindrical layer. This type of surface represents a considerable portion of reaction sites in porous electrodes due to the requirement of percolation passages for oxygen/ion transport. Following the morphology depicted in Fig. 5(a), the cylindrical-layer thickness can be derived as:

$$l = \left(1 - \sqrt{\frac{\varepsilon_p - \varepsilon_{prod}}{\varepsilon_p}}\right) r_p \tag{15}$$

where ε_p is the porosity of pore space, ε_{prod} the volume fraction of discharge product, and r_p the radius of a cylindrical channel. Assuming the resistance ($\Omega\,m^2$) is proportional to the film thickness:

$$R_{prod} = A_0 l + R_0 = A_0 \left(1 - \sqrt{\frac{\varepsilon_p - \varepsilon_{prod}}{\varepsilon_p}}\right) r_p + R_0 \tag{16}$$

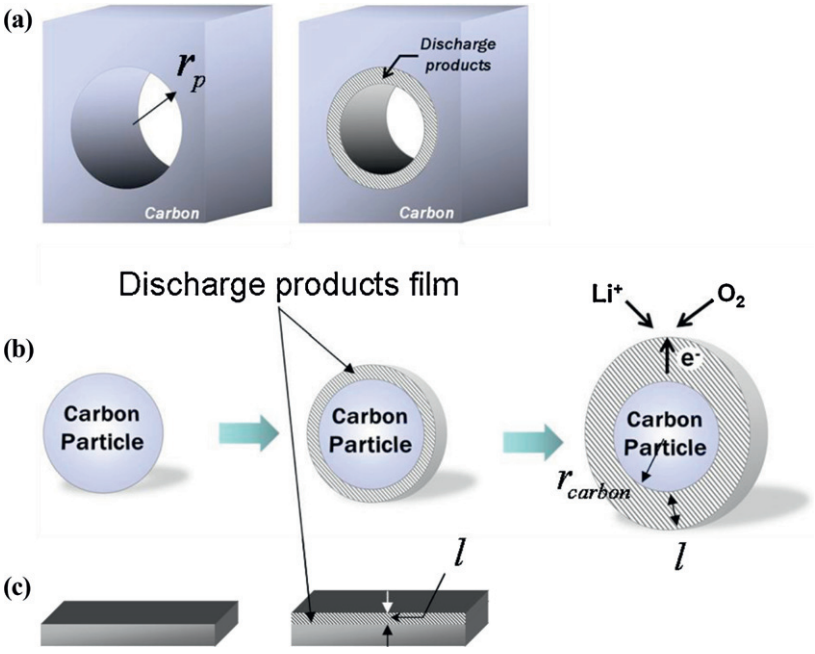

Fig. 5. Various growth modes of discharge product: (a) the cylindrical-film growth mode; (b) the spherical-film growth mode; (c) the planar-film growth mode [27].

where R_0 is the contact resistance between the carbon particle and deposit shell. This resistance increases the ohmic voltage loss at the reaction surface, and the surface discharge overpotential can be modified by:

$$\eta = \Phi^{(s)} - \Phi^{(m)} - U_0 - i_n R_{prod} \tag{17}$$

where i_n is the current density across the discharge film at the direction normal to the reaction surface. Therefore, the voltage loss due to the resistive layer can be written as:

$$\Delta\eta = -i_n R_{prod} = -\frac{I}{a}\left(A_0\left(1-\sqrt{\frac{\varepsilon_p-\varepsilon_{prod}}{\varepsilon_p}}\right)r_p + R_0\right) \tag{18}$$

The above assumes a uniform current density across the cathode electrode:

$$I = -\int_0^{\delta_c} j_c dy = j_c\delta_c \tag{19}$$

The volume fraction of the discharge product ε_{prod} can be calculated by integrating its production rate:

$$\varepsilon_{prod} = \int_0^t -\frac{j_c M_{prod}}{nF\rho_{prod}}dt = \frac{IM_{prod}}{n\delta_c F\rho_{prod}}t \tag{20}$$

where n is the moles of electron transferred per mole of the product. The coulomb of discharge Q per area (mA h/cm^2) can be defined as the amount of the produced charge per area and is a function of the current density I:

$$Q = \int_0^t Idt \overset{I=\text{constant}}{\longrightarrow} Q = I\times t \tag{21}$$

Thus the relationship between the discharge overpotential and Q is:

$$\Delta\eta = -\frac{I}{a}\left(A_0\left[1-\sqrt{1-\frac{QM_{prod}}{nF\delta_c\rho_{prod}\varepsilon_p}}\right]r_p + R_0\right) \tag{22}$$

The discharge capability can then be evaluated when the cut-off voltage is given (usually 2.0 V).

3.1.2. Spherical-film growth mode

Carbon particles (e.g. super carbon) are a common cathode material. The particles can be assumed as perfect spheres with their dimensions r_{carbon} following the particle size distribution determined by the fabrication detail. Assuming the discharge products are deposited over a spherical surface, a resistor shell will form. The shell thickness can be calculated from its morphology:

$$l = \left(\sqrt[1/3]{\frac{\varepsilon_{carbon}+\varepsilon_{prod}}{\varepsilon_{carbon}}} - 1\right)r_{carbon} \tag{23}$$

Note that the above equation was also presented by Ref. [11] in their analysis. The voltage loss can then be calculated by:

$$\Delta\eta = \frac{I}{a}\left(A_0\left[\sqrt[1/3]{1+\frac{QM_{prod}}{\varepsilon_{carbon}nF\delta_c\rho_{prod}}} - 1\right]r_{carbon} + R_0\right) \tag{24}$$

3.1.3. Planar-film growth mode

Flat electrodes are frequently used in experiment, where the discharge product forms a planar layer. This morphology may be encountered in large-size pores in porous electrodes where the surface curvature is negligibly small. In this growth mode, the film thickness is directly determined by the discharge product volume:

$$l = \frac{QM_{prod}}{nF\rho_{prod}} \tag{25}$$

therefore the voltage loss becomes:

$$\Delta\eta = -I\left(\frac{A_0 QM_{prod}}{nF\rho_{prod}} + R_0\right) \tag{26}$$

The above shows a linear relationship between the voltage loss and Q when the resistance is assumed to be proportional to the film thickness.

3.2. Reaction surface coverage model

In addition to the added electric resistance, the discharge deposit can impact battery performance through other mechanisms, such as the reduced reactive surface area (see Fig. 4), and enlarged oxygen/ion transport resistance due to shrink pore passages (see Fig. 5(a)). One active area of relevant research is the ice precipitation inside PEM fuel cells during subfreezing operation. In PEM fuel cells, water is produced in cathode electrode and will freeze under subzero temperature. The produced ice is deposited at the local reaction surface, blocking oxygen transport passage and covering the active catalyst surface. The effect results in cell voltage loss and eventually shuts down fuel cell operation when ice buildup reaches a critical level [19]. The pattern of voltage drop in PEM fuel cell during subfreezing operation is similar to that of Li-air batteries: both exhibit a flat change at the beginning, followed by a fast drop at the latter stage. In PEM fuel cells, the effects of ice formation can be delineated by two major mechanisms [18]: one is the ice coverage over the reaction surface (the associated voltage loss $\Delta\eta_{c,1}$), the other is the blockage of oxygen passage (the associated voltage loss $\Delta\eta_{c,2}$). As to the former, bulk ice nucleates at the reaction surface, cutting off the oxygen access. The coverage effect can be accounted for by modifying the surface to volume ratio and consequently the Butler–Volmer equation is rewritten as [18]:

$$j = -ai_{0,c}^{ref}\frac{C^{O_2}}{C^{O_2,ref}}\exp\left(-\frac{(1-\beta)F}{RT}\cdot\eta\right) \quad \text{or}$$

$$j = -a_0(1-s_{ice})^{\tau_a} i_{0,c}^{ref}\frac{C^{O_2}}{C^{O_2,ref}}\exp\left(-\frac{(1-\beta)F}{RT}\cdot\eta\right) \tag{27}$$

where s_{ice} is defined as the ice volume fraction in open pores, and the associated voltage loss can be expressed by [18]:

$$\Delta\eta_{c,1} = \frac{RT\tau_a}{\alpha_c F}\ln(1-s_{ice}) \tag{28}$$

where the subscript c denotes the cathode. Similar to the surface coverage model in PEM fuel cells, the effect of discharge precipitates over the carbon surface in Li-air batteries can be formulated by:

$$j_c = -a\left(1-\frac{\varepsilon_{prod}}{\varepsilon}\right)^{\tau_a} i_{0,c}^{ref} C_{O_2}^{1-\beta} C_{Ce}^{1-\beta}\exp\left(-\frac{1-\beta}{RT}F\eta\right) \tag{29}$$

where ε is the electrode porosity, and the overpotential can be written as:

$$\eta = \eta_0 + \Delta\eta = \Phi^{(s)} - \Phi^{(m)} - U_0 + \Delta\eta \tag{30}$$

where $\Delta\eta$ denotes the added voltage loss caused by the discharge product presence only. For the battery operation at constant current density (or j_c is constant given no spatial variation of local reaction rate), the above yields:

$$j_c = j_c^0\left(1-\frac{QM_{prod}}{nF\varepsilon\delta_c\rho_{prod}}\right)^{\tau_a}\exp\left(-\frac{1-\beta}{RT}F\Delta\eta\right) \tag{31}$$

where j_c^0 represents the initial current density when no product is present or $\varepsilon_{prod} = 0$ and $\Delta\eta = 0$. Canceling j_c and j_c^0 leads to:

$$\Delta\eta = -\frac{\tau_a RT}{(1-\beta)F}\ln\left(1-\frac{QM_{prod}}{nF\varepsilon\rho_{prod}\delta_c}\right) \tag{32}$$

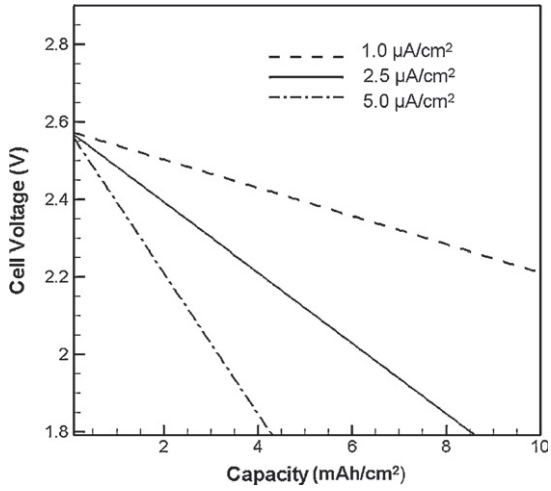

Fig. 6. Discharge curves for the planar-film growth mode, predicted by Eq. (26).

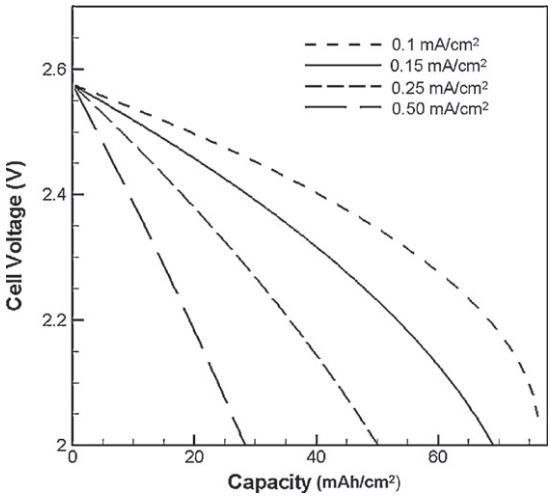

Fig. 8. Discharge curves for the cylindrical-film growth mode, predicted by Eq. (22).

Our previous paper points out that the coefficient τ_a may not be a constant due to the nature of the heterogeneous deposit precipitation, and a varying τ_a yields a good match with experimental data [17]. In addition, the coverage model presented above is more general, encompassing the film resistor model. Adopting the spherical-film growth mode we can equate Eqs. (32) and (24), will yield:

$$\tau_a = -\frac{I(1-\beta)F}{aRT\ln\left(1-\frac{\varepsilon_{prod}}{\varepsilon}\right)}\left\{A_0\left[\sqrt[1/3]{1-\frac{\varepsilon_{prod}}{\varepsilon_{carbon}}}-1\right]r_{carbon}+R_0\right\} \quad (33)$$

The above shows that the coefficient τ_a is proportional to the current density I and is a function of ε_{prod}.

4. Results and discussion

Fig. 6 shows the discharge voltage evolution for the planar growth mode. Eq. (26) is used for the prediction with the values of the used parameters listed in Table 1. It indicates a linear relationship between the voltage loss and discharging capacity, as expected. This trend qualitatively shows the effects of the product precipitation on discharging voltage observed experimentally. At higher current, the voltage loss speeds up, reducing the capacity. The figure, however, indicates that the predictions fail to match with the experimental observations in terms of the voltage drop rates at the beginning and latter stages. Specifically, experiment shows a slow voltage drop rate at the beginning, followed by a rapid fall at the latter stage, see Fig. 2. The predicted curve, however, shows no change in the dropping rate for the two stages.

Figs. 7 and 8 display the results for the spherical- and cylindrical-film growth modes, predicted by Eqs. (24) and (22), respectively. It can be seen that the spherical-film growth mode indicates the predicted latter-stage trend is opposite to experimental observation: the voltage drop slows down at the latter stage. In contrast, the one for the cylindrical-film mode exhibits a trend closer to experimental observation: a faster drop of voltage at the latter stage. It is evident that the growth-mode geometrical feature influences the effect of discharge product on battery performance. Note that the predictions of the cylindrical mode are not yet satisfactory to match with experimental data, particularly at various currents. In reality, a porous electrode consists of a number of channels with various dimensions as well as different surface morphologies, and the overall effects observed experimentally in such porous electrodes likely result from the combined effects of all the constituent surface features.

As to the spherical-film growth mode, Ref. [11] proposed a similar approach. To match with experimental data, they assumed an empirical relationship between the thickness and electric resistance, which is determined through comparing with the

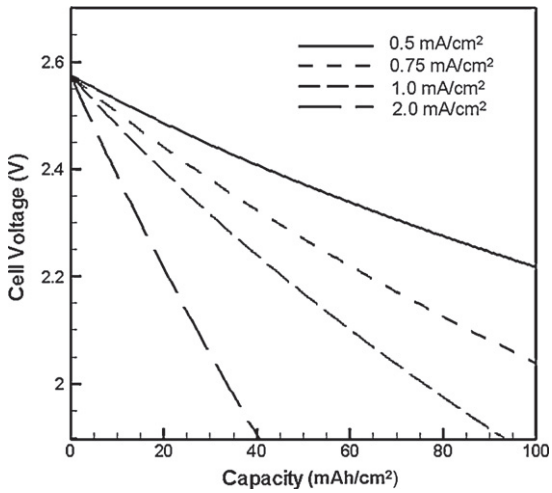

Fig. 7. Discharge curves for the spherical-film growth mode, predicted by Eq. (24).

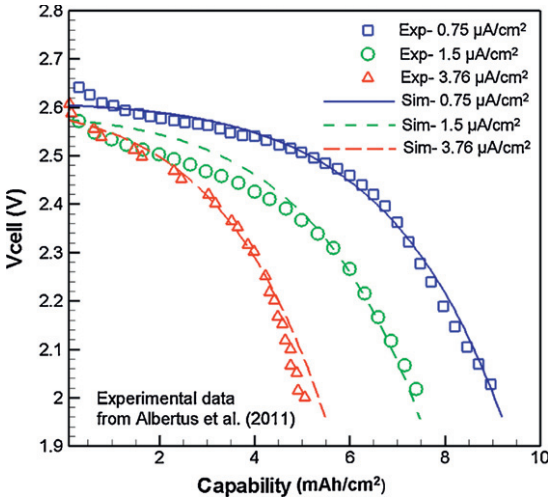

Fig. 9. Comparison of experimental data and model prediction using the model of the planar-film-growth mode with the empirical resistance of Eq. (35).

Table 1
Physical, electrochemical, and model parameters.

Description	Unit	Value
Temperature	°C	25
Transfer coefficient, β		0.5
Faraday constant	C/mol	96,487
Electrical conductivity of cathode electrode	S/m	~10
O_2 diffusivity in electrolyte [10]	cm^2/s	4×10^{-5} in DME with of 1 M Li^+ 2.2×10^{-6} in PC of 1 M Li^+
O_2 solubility [8]		0.00876 in DME with of 1 M Li^+ 0.0021 in PC of 1 M Li^+
Cathode thermal conductivity [16,18]	W/(m K)	~1.0
Tortuosity τ [18]		1.5
Cathode electrode porosity		0.9
Spherical particle size, r_{carbon} [11]	nm	40
Cylindrical channel dimension, r_p	nm	100
Density of discharge product (Li_2O_2/Li_2CO_3)	kg/m^3	2140/2110
Molecular weight of discharge product (Li_2O_2/Li_2CO_3)	kg/mol	0.04588/0.07389
The surface-to-volume ratio a [18]		100–1000
c_1 in Eq. (35) [11]	m^{-1}	4.7×10^7
A_0	$\Omega\,m^2$	8.5×10^7
B_1 in Eq. (36)		2.5
B_2 in Eq. (36) (Ref. [17] used a value of around 7 if using s_0 of 0.4)		8
s_0 in Eq. (36)		0.4

measured voltage loss. The following exponential relationship was adopted:

$$R_{prod} = l \exp(c_1 l + c_2) \quad (34)$$

The above shows a rapid increase of resistance with the film thickness. To match with the experimental data using the present model of planar growth mode, we use a similar exponential form of the film resistance–thickness relationship as follow:

$$R_{prod} = A_0 \exp(c_1 l) \quad (35)$$

where the coefficient c_1 is the same as that used in Ref.[11], see Table 1. Fig. 9 displays the model prediction using the above resistance correlation. In contrast to the previous prediction in Fig. 6, a fast loss is indicated at the latter stage, and a satisfactory agreement with experimental data is achieved for all the three current densities. Note that the experimental data used were obtained using flat electrodes, which exactly fit in the planar growth mode.

Fig. 10 displays the coverage model prediction using a coverage coefficient that is dependent on the current density only. The current-density dependence of the coefficient is derived from Eq. (33), which shows a linear change with current. The predicted curves show a drop at an increasing rate in the latter stage for most cases. However, at the highest current the curve changes nearly linearly with the amount of the charge produced, which deviates from observed experimental trends. To bring the coverage model predictions closer to the experimental data, we adopted the form of the coverage coefficient as a function of the product volume fraction similar to that in PEM fuel cell, see Fig. 4(d), where the coefficient is constant initially and starts to change linearly with the product volume fractions, i.e.

$$\tau_a = \begin{cases} B_1 \dfrac{I}{I_0} & s < s_0 \text{ where } s = \dfrac{\varepsilon_{prod}}{\varepsilon} \\ \dfrac{I}{I_0}(B_1 + B_2(s - s_0)) & \text{otherwise} \end{cases} \quad (36)$$

we arbitrarily set a value of s_0 to best match the experimental data, see Table 1. The chosen value of B_2 is close to that in Ref. [17] (which is around 7) if s_0 is set to the value in the present paper. Fig. 11 compares the coverage model prediction with the experimental

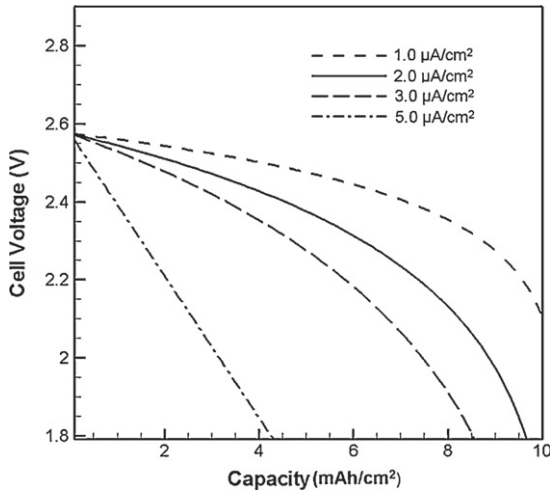

Fig. 10. Model prediction by the coverage model with a constant coverage coefficient (Eq. (32)).

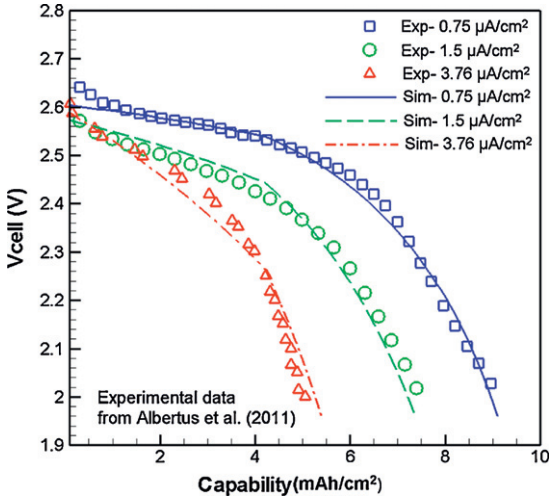

Fig. 11. Comparison of experimental data and model prediction using the coverage model with a coverage coefficient varying with the volume fraction of the discharge product (Eq. (36)).

data. A satisfactory agreement is achieved for all the current densities. This clearly indicates the similarity between the ice formation phenomenon in PEM fuel cells and discharge precipitation in Li-air batteries.

5. Conclusions

In this work, a modeling study is presented on the discharge product formation and effects in the cathode of Li-air batteries. We first present an analysis to evaluate the spatial variations of important quantities including temperature, species concentrations, and phase potentials. We found that the degree of variations can be controlled by adjusting the discharge current dentistry and cathode thickness: for sufficiently small current and thickness, the variations can be neglected and the reaction can be assumed uniform across the cathode. Three deposit-growth modes were analyzed and compared, and the voltage loss associated with each mode was derived. The predictions qualitatively show the trend of discharge voltage observed experimentally, but fail to match with the data quantitatively. By assuming an empirical relationship between the film thickness and electric resistance, a satisfactory agreement between the prediction and experimental data was achieved at various currents. We also demonstrated the similarity of the icing phenomena in PEM fuel cells and discharge product precipitation in Li-air batteries. Following the ice-deposit theory in PEM fuel cell, we proposed a coverage model to account for the effects of discharge precipitations in Li-air batteries. The results were compared with experimental data available in the literature, and a satisfactory agreement was achieved by using the coverage coefficient similar to that in PEM fuel cells, which indicates the similarity between ice formation in PEM fuel cells and insoluble products in Li-air batteries.

Acknowledgements

Partial support by the Academic Senate Council on Research, Computing and Library Resources of the UC Irvine is gratefully acknowledged.

Appendix A. Nomenclature

a	factor of effective catalyst area per unit volume when discharge product is present
a_0	factor of catalyst surface area factor per unit volume
C	molar concentration of species k, mol/m^3
D	species diffusivity, m^2/s
F	Faraday's constant, 96,487 C/equivalent
I	current density, A/cm^2
i	superficial current density, A/cm^2
j	transfer current density, A/cm^3
M	molecular weight, kg/mol
R	universal gas constant, 8.134 J/(mol K); ohmic resistance, mΩ cm^2
s_{ice}	ice volume fraction
t	time, s
T	temperature, K
U_0	equilibrium potential, V

Greek

β	transfer coefficient
ρ	density, kg/m^3
ϕ	phase potential, V
κ	ionic conductivity, S/m
ε	porosity or volume fraction
η	surface overpotential, V
τ	tortuosity/coverage coefficient
δ	thickness, m

Superscripts and subscripts

abs	absorption
c	cathode
d	diffusion
e	electrolyte
eff	effective value
0	reference value; initial value

References

[1] G. Girishkumar, B. McCloskey, A.C. Luntz, S. Swanson, W. Wilcke, Lithium-air battery: promise and challenges, Journal of Physical Chemistry Letters 1 (2010) 2193–2203.
[2] K. Kinoshita, Metal/air batteries, in: K. Kinoshita (Ed.), Electrochemical Oxygen Technology, John Wiley & Sons, Inc., New York, 1992.
[3] K.M. Abraham, Z. Jiang, A polymer electrolyte-based rechargeable lithium/oxygen battery, Journal of the Electrochemical Society 143 (1996) 1–5.
[4] A. Débart, J. Bao, G. Armstrong, P.G. Bruce, Journal of Power Sources 174 (2007) 1177.
[5] Y. Lu, Z. Xu, H.A. Gasteiger, S. Chen, K. Hamad-Schifferli, Y. Shao-Horn, Journal of the American Chemical Society 132 (2010) 12170.
[6] M. Mirzaeian, P.J. Hall, Electrochimica Acta 54 (2009) 7444.
[7] Y. Lu, H.A. Gasteiger, M.C. Parent, V. Chiloyan, Y. Shao-Horn, Electrochemical and Solid-State Letters 13 (2010) A69.
[8] J. Read, K. Mutolo, M. Ervin, W. Behl, J. Wolfenstine, A. Driedger, D. Foster, Journal of the Electrochemical Society 150 (2003) A1351–A1356.
[9] S.S. Zhang, D. Foster, J. Read, Journal of Power Sources 195 (2010) 1235.
[10] Y.C. Lu, D.G. Kwabi, K.P.C. Yao, J.R. Harding, J. Zhou, L. Zuin, Y. Shao-Horn, Energy & Environmental Science 4 (2011) 2999–3007.
[11] P. Albertus, G. Girishkumar, B. McCloskey, R.S. Sánchez-Carrera, B. Kozinsky, J. Christensen, A.C. Luntz, Identifying capacity limitations in the Li/oxygen battery using experiments and modeling, Journal of the Electrochemical Society 158 (2011) A343–A351.
[12] V. Viswanathan, K.S. Thygesen, J.S. Hummelshøj, J.K. Nørskov, G. Girishkumar, B.D. McCloskey, A.C. Luntz, Electrical conductivity in Li_2O_2 and its role in determining capacity limitations in non-aqueous Li–O_2 batteries, Journal of Chemical Physics 135 (2011) 214704.
[13] R.R. Gagne, A. Carl, Koval, C. George, Lisensky, Ferrocene as an internal standard for electrochemical measurements, Inorganic Chemistry 19 (9) (1980) 2854–2855.
[14] M. Uiberacker, Th. Uphues, M. Schultze, A.J. Verhoef, V. Yakovlev, M.F. Kling, J. Rauschenberger, N.M. Kabachnik, H. Schröder, M. Lezius, K.L. Kompa, H.-G. Muller, M.J.J. Vrakking, S. Hendel, U. Kleineberg, U. Heinzmann, M. Drescher, F. Krausz, Attosecond real-time observation of electron tunnelling in atoms, Nature 446 (2007) 627.
[15] M. Razavy, Quantum Theory of Tunneling, World Scientific Publishing Co., 2003.
[16] Y. Wang, K.S. Chen, J. Mishler, S.C. Cho, X.C. Adroher, A review of polymer electrolyte membrane fuel cells: technology, applications, and needs on fundamental research, Applied Energy 88 (2011) 981–1007.
[17] J. Mishler, Y. Wang, P.P. Mukherjee, R. Mukundan, R.L. Borup, Subfreezing operation of polymer electrolyte fuel cells: ice formation and cell performance loss, Electrochimica Acta 65 (2012) 127–133.
[18] Y. Wang, Analysis of the key parameters in the cold start of polymer electrolyte fuel cells, Journal of the Electrochemical Society 154 (2007) B1041–B1048.
[19] Y. Wang, P.P. Mukherjee, J. Mishler, R. Mukundan, R.L. Borup, Cold start of polymer electrolyte fuel cells: three-stage startup characterization, Electrochimica Acta 55 (2010) 2636–2644.
[20] G.K. Batchelor, Brownian diffusion of particles with hydrodynamic interaction, Journal of Fluid Mechanics 74 (1976) 1–29.
[21] W.M. Deen, Analysis of Transport Phenomena, Oxford University Press, 1998.
[22] E. Yeager, Dioxygen electrocatalysis: mechanisms in relation to catalyst structure, Journal of Molecular Catalysis 38 (1986) 5–11.
[23] J. Zhang, PEM Fuel Cell Electrocatalysts and Catalyst Layers: Fundamentals and Applications, Springer, 2008.
[24] R.J. Taylor, A.A. Humffray, Electrochemical studies on glassy carbon electrodes: II. Oxygen reduction in solutions of high pH (pH > 10), Journal of Electroanalytical Chemistry 64 (1975) 63–84.
[25] R.J. Taylor, A.A. Humffray, Electrochemical studies on glassy carbon electrodes: II. Oxygen reduction in solutions of low pH (pH < 10), Journal of Electroanalytical Chemistry 64 (1975) 85–94.
[26] S. Sandhu, J. Fellner, G. Brutchen, Journal of Power Sources 164 (2007) 365.
[27] S.C. Cho, Y. Wang, private communication.